NJC

Accepted Manuscript

This article can be cited before page numbers have been issued, to do this please use: M. Das, R. Herchel, Z. Travnicek, V. Bertolasi and D. Ray, *New J. Chem.*, 2018, DOI: 10.1039/C8NJ03269F.

ROYAL SOCIETY OF CHEMISTRY

rsc.li/njc

ROYAL SOCIETY OF CHEMISTRY
View Article Online
DOI: 10.1039/C8NJ03269F

Journal Name

ARTICLE

Anion Coordination Directed Synthesis Patterns for [Ni_4] Aggregates: Structural Changes for Thiocyanate Coordination and Ligand Arm Hydrolysis

Received 00th January 20xx,
Accepted 00th January 20xx

DOI: 10.1039/x0xx00000x

www.rsc.org/

Manisha Das,[a] Radovan Herchel,[b] Zdeněk Trávníček,[b] Valerio Bertolasi,[c] and Debashis Ray*[,a]

Coordination reactivity of ligand H_5L1 (2,6-bis-{(1,3-dihydroxy-2-methylpropan-2-ylimino)methyl}-4-methylphenol) toward nickel(II) ions in presence of two different anions resulted cubane and fused dicubne type of tetranuclear coordination aggregates. In the first case utilization of two carboxylate (R = Me and Et in RCO_2^-) anions led to cubane type Ni_4O_4 aggregates $[Ni_4(H_4L1)_2(\mu_3\text{–}OH)_2(\mu_{1,3}\text{–}O_2CCH_3)_2](NO_3)(CH_3COO)\cdot 3H_2O$ (**1**) and $[Ni_4(H_4L1)_2(\mu_3\text{–}OH)_2(\mu_{1,3}\text{–}O_2CC_2H_5)_2](NO_3)(C_2H_5COO)\cdot CH_3CN\cdot 1.5H_2O$ (**2**). Whereas use of thiocyanate anions triggered single imine arm hydrolysis of H_5L1 and gave partial dicubane type $Ni_4N_2O_4$ aggregates $[Ni_4(H_2L2)_2(HAMP)_2(\mu_{1,1}\text{-}NCS)_2](NO_3)_2$ (**3a**) and $[Ni_4(H_2L2)_2(HAMP)_2(\mu_{1,1}\text{-}NCS)_2]Cl_2\cdot CH_3OH\cdot H_2O$ (**3b**) (H_2L2 = 3-{(1,3-dihydroxy-2-methylpropan-2-ylimino)methyl}-2-hydroxy-5-methylbenzaldehyde). Liberated 2-amino-2-methyl-1,3-propanediol from imine arm hydrolysis was successfully trapped in **3a** and **3b** for the growth and stabilization of different molecular architecture. Mass spectral evidences estabilied that two types of dinuclear fragments $Ni_2(H_4L1)$ and $Ni_2(H_2L2)$, from originally used and partially hydrolyzed ligand anions have been self-assembled for two types of Ni^{II} based coordination aggregates. Two sets of complexes were characterized by elemental analysis, FT-IR and optical spectroscopy, variable temperature magnetic measurements, and single crystal X-ray analysis. Magnetic behavior examined through the temperature interval of 1.9 – 300 K using experimental and theoretical corroborations support the exchange pathways within the two types of [Ni_4] coordination aggregates.

Introduction

Design and synthesis of a new ligand system always rely on its reactivity toward chosen metal ions to provide metal ions bound forms. The nature and solution stability of the immediately formed fragments, in presence/absence of bound small molecules or anions, is crucial for their survival in solution and separation as discrete metal ion complexes. On the other hand these fragments can show reactivity for self-aggregation to result coordination aggregates. The resulting species are important to similar structural motifs, occasionally found in biology and discovery of new structural forms for structure dependent magnetic interactions between the paramagnetic centres attached to the ligand. Phenol-based Schiff bases are interesting in this regard for their supportive role in bridging two metal ions in close proximity, required for catalytic functions and magnetic spin exchange. In recent years synthesis and characterization of high-nuclearity nickel(II) complexes have shown promise due to their relevance to biologically significant motifs and potential as magnetic materials.[1] In the former area, two adjacent paramagnetic Ni^{II} centers were needed for enzymatic activity such as in Urease, where the substrate urea is hydrolyzed by the nucleophilic attack of nickel(II) ion bound hydroxide ion to the carbonyl carbon atom.[2] Ni^{II} ion bound H_2O or HO^- groups are superior nucleophile for hydrolysis reactions to occur and can hydrolyze in a similar fashion the Schiff bases having imine side-arms as reported in the present investigation.[3] Removal of one imine side-arm provides mono-imine Schiff base ligand, otherwise unachievable during synthesis.[4] The coordination aggregates thus obtained can further add to the growing family of Ni^{II} ion based magnetic materials useful for many applications.[5] Incorporation of Ni^{II} ion is interesting in the synthesis of molecule-based magnets[6] and development of spin-phonon traps.[7] Studies on [Ni_4] coordination aggregates are thus interesting for possible switching of the spin ground states between S_T = 4 and S_T = 0.[8] Identification of enhanced magnetocaloric effect (MCE) within such systems can have use in cooling applications.[9] Generation of ligand-bound {Ni_2} fragments and their stabilization in solutions were thus

[a] Department of Chemistry, Indian Institute of Technology, Kharagpur 721 302, India. E-mail: dray@chem.iitkgp.ac.in; Fax: (+91)3222-82252; Tel: (+91)3222-83324
[b] Division of Biologically Active Complexes and Molecular Magnets, Regional Centre of Advanced Technologies and Materials, Faculty of Science, Palacký University in Olomouc, 783 71 Olomouc, Czech Republic
[c] Dipartimento di Scienze Chimiche e Farmaceutiche, Centro di Strutturistica Diffrattometrica, University of Ferrara, 44121 Ferrara, Italy

†Electronic Supplementary Information (ESI) available: [Solid State FTIR Identification, Powder X-ray Diffraction Patterns, EPR Spectra, Scheme S1-S2, Chart S1–S2, Figures S1–S16, Tables S1–S3.
X-ray crystallographic data in CIF format, CCDC 1835111, 1835112, 1835113 and 1835110 contain the supplementary crystallographic data in CIF format for complexes **1**–**3b**.]. See DOI: 10.1039/x0xx00000x

important for fine tuning and monitoring the follow up aggregation reactions involving two or more ancillary bridges from outside or generated in the reaction medium. Separate reaction conditions can be chosen to deliver different sets of bridges derived from solvent, metal ion salts or external addition. Bridges like HO^-, RO^-, RCO_2^-, N_3^-, SCN^- are known to support cubane,[10] stepped cubane,[11] partial dicubane and other higher order structures through such aggregation reactions (Scheme S1 in ESI†).[12]

As ancillary donor, the carboxylate groups have the aggregate supporting potential to bridge two metal ion centers *via* $\mu_{1,1}$ in *syn-anti* mode, $\mu_{1,3}$ in *syn-syn*, *syn-anti*, and *anti-anti* mode, $\mu_{1,1,3}$ in *anti-syn-syn* and *anti-syn-anti* mode, and $\mu_{1,1,3,3}$ in *syn-anti-syn-anti* mode. HO^- and RO^- anions can expand their bridging capacity to bring more number of ligand bound metal ions together for aggregation.[13,14,15] Unlike the N_3^- ions, the SCN^- ions are not very much effective in promoting such bridging activity to give multimetallic coordination aggregates, chains and sheets.[16,17] SCN^- ions can show μ_1, $\mu_{1,1}$ or $\mu_{1,3}$ modes of binding.[13,18,19] As a ligand amino propanediol can bridge two or more metal ions through its amine and alcohol functions. Tripodal-bridging feature by this ligand is known in two cases.[20,21]

In this background, we were interested to explore the coordination ability of H_5L1 (2,6-bis-{(1,3-dihydroxy-2-methylpropan-2-ylimino)methyl}-4-methylphenol) (Chart S1 in ESI†, left) with nickel(II) salts. Coordination modes of ligands (H_4L1^-, H_2L2^-), diol amine ($HAMP^-$), auxiliary anions (RCO_2^-, SCN^-) and HO^- groups established in this work are depicted in Chart S2 (ESI†).

Bridging capacity of HO^- vs. SCN^- and RCO_2^- vs. $HAMP^-$ has been examined for two different types of molecular aggregation reported in this work. The work also showed the importance of partially filled coordination environment around the pro-octahedral nickel(II) ions for aggregation and susceptibility for the imine arm hydrolysis (Scheme 1). The combinations of HO^- and RCO_2^- ions are involved in $[Ni_4(H_4L1)_2(\mu_3\text{–}OH)_2(\mu_{1,3}\text{–}O_2CCH_3)_2](NO_3)(CH_3COO)\cdot 3H_2O$ (**1**) and $[Ni_4(H_4L1)_2(\mu_3\text{–}OH)_2(\mu_{1,3}\text{–}O_2CC_2H_5)_2](NO_3)(C_2H_5COO)\cdot CH_3CN\cdot 1.5H_2O$ (**2**), and SCN^- and $HAMP^-$ groups are chosen for $[Ni_4(H_2L2)_2(HAMP)_2(\mu_{1,1}\text{-}NCS)_2](NO_3)_2$ (**3a**) and $[Ni_4(H_2L2)_2(HAMP)_2(\mu_{1,1}\text{-}NCS)_2]Cl_2\cdot CH_3OH\cdot H_2O$ (**3b**). Synthesis and details of molecular structures have been compared in this work, and their individual magnetic behaviour has been examined.

Scheme 1 Coordination driven imine arm hydrolysis

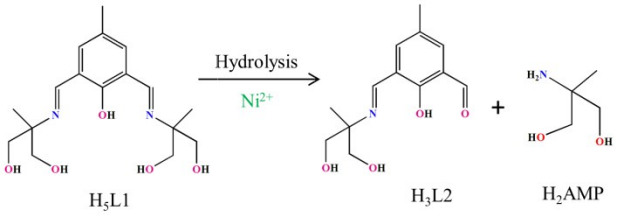

Results and discussion

Synthetic Protocol

H_5L1 was obtained from a reaction of 2,6-diformyl-4-methylphenol and 2-amino-2-metyhl-1,3-propanediol in 1:2 molar ratio (Scheme S2 in ESI†). Separate reactions with nickel(II) nitrate and nickel(II) chloride were explored to identify the role of externally added ancillary groups (Scheme 2). Reaction of $Ni(NO_3)_2\cdot 6H_2O$ with H_5L1, ancillary ligands (from sodium carboxylates or ammonium thiocyanate) and NEt_3 in MeOH-MeCN (1:10) gave **1**, **2** and **3a**, whereas use of $NiCl_2\cdot 6H_2O$ provided **3b** in MeOH. **1** was obtained as green crystals in 71% yield from a greenish solution followed by solvent evaporation (eq 1).

$$4Ni(NO_3)_2\cdot 6H_2O + 2H_5L1 + 4CH_3COONa + 3NEt_3 \xrightarrow{CH_3CN-CH_3OH} [Ni_4(H_4L1)_2(\mu_3-OH)_2(\mu_{1,3}-O_2CCH_3)_2](NO_3)(CH_3COO)\cdot 3H_2O + 3(NHEt_3)(NO_3) + CH_3COOH + 4NaNO_3 + 19H_2O \cdots (1)$$

Incorporation of propionate ions provided **2** as green crystals from the reaction mixture in 69% yield (eq 2).

$$4Ni(NO_3)_2\cdot 6H_2O + 2H_5L1 + 4C_2H_5COONa + 3NEt_3 + CH_3CN \xrightarrow{CH_3CN-CH_3OH} [Ni_4(H_4L1)_2(\mu_3-OH)_2(\mu_{1,3}-O_2CC_2H_5)_2](NO_3)(C_2H_5COO)\cdot CH_3CN\cdot 1.5H_2O + 3(NHEt_3)(NO_3) + C_2H_5COOH + 4NaNO_3 + 20.5H_2O \cdots (2)$$

Utilization of nitrogen ends of thiocyanate ions for nickel(II) coordination triggered single imine arm hydrolysis and liberation of amine alcohol for entrapment in anionic form resulting **3a** in 72 % yield (eq 3).

$$4Ni(NO_3)_2\cdot 6H_2O + 2H_5L1 + 2NH_4SCN + 6NEt_3 \xrightarrow{CH_3OH-CH_3CN} [Ni_4(H_2L2)_2(HAMP)_2(\mu_{1,1}-NCS)_2](NO_3)_2 + 6(NHEt_3)(NO_3) + 2NH_4OH + 21H_2O \cdots (3)$$

Chloride salt **3b** was isolated in 72% yield from the same reaction with $NiCl_2\cdot 6H_2O$ (eq 4). Initial identification of $[Ni_4(H_2L2)_2(HAMP)_2(\mu_{1,1}\text{–}NCS)_2]Cl_2\cdot CH_3OH\cdot H_2O$ was made through elemental analysis, conductivity measurements and spectral studies.

$$4NiCl_2\cdot 6H_2O + 2H_5L1 + 2NH_4SCN + 6NEt_3 + CH_3OH \xrightarrow{CH_3OH} [Ni_4(H_2L2)_2(HAMP)_2(\mu_{1,1}-NCS)_2]Cl_2\cdot CH_3OH\cdot H_2O + 6(NHEt_3)Cl + 2NH_4OH + 20H_2O \cdots (4)$$

In all the above cases presence of NEt_3 is crucial. Other bases such as NaOMe, or NaOEt gave intractable gummy masses not suitable for routine characterizations.

View Article Online
DOI: 10.1039/C8NJ03269F

Scheme 2 Synthetic routes for **1**–**3b**

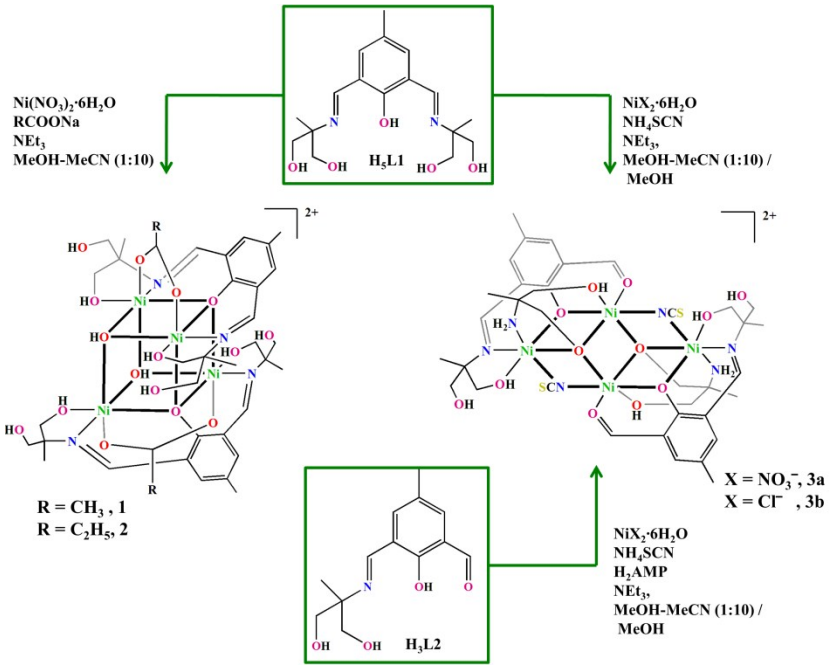

Electronic Spectral Transitions in Solution

Characterizations for the metal ion environments in 1200 to 200 nm range in MeOH for **1**–**3b** gave characteristic signature electronic absorption bands (Figure S3, ESI†). For the entire family (**1**, **2**, **3a** and **3b)**, absorption bands (λ_{max}) at 622 nm (ε = 26 L mol^{-1} cm^{-1}), 622 nm (ε = 26 L mol^{-1} cm^{-1}), 596 nm (ε = 40 L mol^{-1} cm^{-1}) and 592 nm (ε = 20 L mol^{-1} cm^{-1}), are assigned to the spin-allowed $^3A_{2g}(F) \rightarrow {}^3T_{1g}(F)$ transitions for Ni^{II} centers in distorted octahedral environments.[22] Even if the coordination aggregates are not stable in solution, the signatures for both octahedral and pro-octahedral environments are seen. The lowest energy $^3A_{2g}(F) \rightarrow {}^3T_{2g}(F)$ transition bands appeared at 994 nm (ε = 38 L mol^{-1} cm^{-1}), 994 nm (ε = 36 L mol^{-1} cm^{-1}), 983 nm (ε = 39 L mol^{-1} cm^{-1}) and 974 nm (ε = 16 L mol^{-1} cm^{-1}), whereas the $^3A_{2g}(F) \rightarrow {}^3T_{1g}(P)$ transitions could not be located with certainty due to overlap with $PhO^- \rightarrow Ni^{II}$ LMCT transitions at 368 nm (ε = 10200 L mol^{-1} cm^{-1}), 368 nm (ε = 8000 L mol^{-1} cm^{-1}), 395 nm (ε = 8500 L mol^{-1} cm^{-1}) and 395 nm (ε = 5400 L mol^{-1} cm^{-1}) for **1**, **2**, **3a** and **3b** respectively. A shoulder at 760 nm (ε = 10 L mol^{-1} cm^{-1}) and 762 nm (ε = 10 L mol^{-1} cm^{-1}) of very low intensity for **1** and **2** were due to the spin forbidden $^3A_{2g}(F) \rightarrow {}^1E_g(F)$ transitions.[23] The intense absorptions at 256 nm (ε = 46500 L mol^{-1} cm^{-1}), 256 nm (ε = 39700 L mol^{-1} cm^{-1}), 251 nm (ε = 24000 L mol^{-1} cm^{-1}) and 251 nm (ε = 16400 L mol^{-1} cm^{-1}) are of ligand origin and can be assigned to intraligand $\pi \rightarrow \pi^*$ transitions.[24]

Description of the Crystal Structures

Single crystals of **1** and **2** were obtained after 1 week by slow evaporation of MeCN-MeOH (10:1) reaction mixture. For **3a** suitable single crystals for X-ray analysis were obtained after 6 days and for **3b** after 12 days from MeOH.

$[Ni_4(H_4L1)_2(\mu_3\text{–}OH)_2(\mu_{1,3}\text{–}O_2CCH_3)_2](NO_3)(CH_3COO)\cdot 3H_2O$ (1) and $[Ni_4(H_4L1)_2(\mu_3\text{–}OH)_2(\mu_{1,3}\text{–}O_2CC_2H_5)_2](NO_3)(C_2H_5COO)\cdot CH_3CN\cdot 1.5H_2O$ (2). Both **1** and **2** crystallizes in triclinic $P\bar{1}$ space group and the significant interatomic parameters are summarized in Table S1 (ESI†). The molecular structures for cationic units of **1** and **2** are shown in Figures 1 and S4 (ESI†). In **1** the asymmetric unit contains one $[Ni_4(H_4L1)_2(\mu_3\text{–}OH)_2(\mu_{1,3}\text{–}O_2CCH_3)_2]^{2+}$ unit, acetate and nitrate anions, and three water molecules. 1+1 combination of nitrate and carboxylate ions were crucial to obtain diffraction quality single crystals.

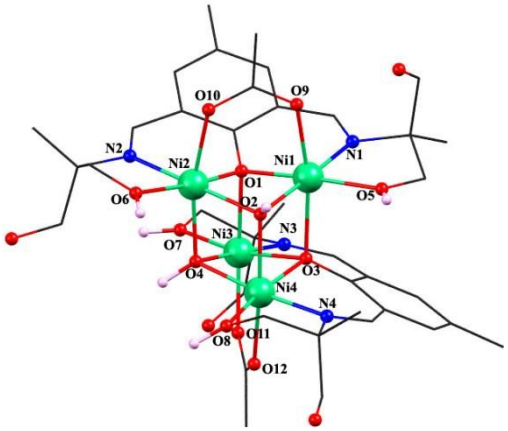

Figure1 Molecular view for the cationic part of **1** with partial atom numbering scheme. Hydrogen atoms are shown only for bridging –OH groups. Counter anions are omitted for clarity. Color code: Ni, green; N, blue; O, red; C, black; H, pink. Ni···Ni distances: Ni1···Ni2, 2.923 Å; Ni3···Ni4, 2.906 Å; Ni1···Ni3, 3.244 Å; Ni1···Ni4, 3.196 Å; Ni2···Ni3, 3.204 Å; Ni2···Ni4, 3.177 Å.

In **2** the asymmetric unit bears one $[Ni_4(H_4L1)_2(\mu_3\text{–}OH)_2(\mu_{1,3}\text{–}O_2CC_2H_5)_2]^{2+}$, one nitrate anion, one propionate anion, one and a half water molecule and an acetonitrile molecule. The $Ni_4(H_4L1)_2(\mu_3\text{–}OH)_2$ aggregate is separated as **1** and **2** from the support of two phenoxido-group bearing ligands and two

solvent water derived HO^- groups. Externally provided carboxylate anions were utilized to cap two opposite faces of the Ni_4 cubic unit and fulfilled the strained NO_5 octahedral geometry around each Ni^{II} center. Hydrogen bonding interactions with dangling alcohol arms give further stabilizations to carboxylate groups. Each H_4L1^- unit provided N_2O_3 donor set to the aggregate from the supports of two solvent water-derived μ_3-OH groups (O2 and O4) located at the two corners of the distorted cube. The Ni–O distances vary within the longer 2.003–2.207 Å range as compared to the Ni–N distances within 1.997–2.022 Å. The phenoxido-bridge mediated Ni–O–Ni angles are in 89.27–99.89° ranges, while the HO^- bridged Ni–O–Ni angles were slightly wider in 91.79–103.76° range. Within the cubic geometry the six Ni···Ni separations along the edges of the Ni_4 tetrahedron vary from 2.906 to 3.244 Å (Figure 1). The nature of donor atoms on the four alternate vertices of the cube dictates the intermetallic separations within the tetrahedral [Ni_4] unit. Thus two phenoxido donor bearing faces register longest Ni···Ni distances of 3.244 and 3.221 Å for **1** and **2**, respectively. Presence of two hydroxido donors gave intermediate Ni···Ni separation of 3.177 and 3.173 Å for **1** and **2** respectively.[25] The third type having phenoxido-hydroxido-bridged structure, with two capping carboxylate anions, gave shortest Ni···Ni separations (2.906 Å and 2.923 Å for **1** and 2.911 and 2.922 Å for **2**). Three distinct types of faces are responsible for the generation of asymmetry in a strained cubic arrangement.

Observation of μ_3-phenoxido supports, as found in **1** and **2**, for fragment aggregation is not so common in comparison to the μ_3-hydroxido/oxido supports. Such μ_3-phenoxido supports have been known for different type of [Ni_4] and [Ni_6] complexes.[3,4]

In case of complex **1**, two discrete molecular units were engaged in intra- as well as intermolecular hydrogen-bonding interactions involving dangling and coordinated hydroxyl groups of the ligand arms and acetate anions (O6–H6···O23, O7–H7···O20, O8–H8···O23, O13–H13···O9 and O15–H15···O11). Specific hydrogen-bond distances are listed in Table S2 (ESI†). The hydroxide bridges within the cubic structure function as hydrogen bond donor and stabilized through hydrogen-bonding interactions with dangling ligand hydroxyl arm (O4–H4···O14) and with nitrate anion (O2–H2···O18). The D···A separations range from 2.564 to 2.947 Å, indicating the presence of both weak and strong types of hydrogen bonding interactions within the crystal lattice (Figure S5 in ESI†). Solvent water molecules were trapped within the crystal lattice due to their involvement in hydrogen bonding interactions with coordinated and dangling hydroxyl group of ligand arm (O5–H5···O1W, O16–H16···O2W).

For **2** the coordinated hydroxyl group of ligand arm was involved in intermolecular hydrogen-bonding interaction with available nitrate and propionate ions (O5–H5···O17, O6–H6···O21, O7–H7···O20, O8–H8···O21). The dangling hydroxyl group of the ligand make intramolecular hydrogen bonding interaction with bridging propionate (O15A–H15A···O11) and intermolecular hydrogen bonding interaction with anionic propionate (O14–H14···O20). The μ_3–OH group of the cubic unit established hydrogen-bonding interaction with dangling ligand hydroxyl group (O4–H4···O14) and with nitrate ion (O2–H2···O18). The water molecules trapped within the crystal lattice participate in active hydrogen-bonding interaction and thus further stabilizes the tetra-nickel aggregate (O1W–H1WA···O12, O13–H13···O1W, O16–H16···O1W) (Figures S6 in ESI†). The D···A separations span a wide range from 2.562 to 2.937 Å, while the D–H···A angles are within 135–174° sustaining variable nature and strength of interaction and cooperatively stabilize the aggregate (Table S2 in ESI†).

$[Ni_4(H_2L2)_2(HAMP)_2(\mu_{1,1}\text{–NCS})_2](NO_3)_2$ (3a) and $[Ni_4(H_2L2)_2(HAMP)_2(\mu_{1,1}\text{–NCS})_2]Cl_2\cdot CH_3OH\cdot H_2O$ (3b). **3a** and **3b** crystallize in monoclinic $P2_1/n$ and triclinic $P\bar{1}$ space groups respectively. Their molecular views are presented in Figures 2 and S7 (ESI†) and the important interatomic parameters are summarized in Table S1 (ESI†). The structure of **3a** consists of one $[Ni_4(H_2L2)_2(HAMP)_2(\mu_{1,1}\text{-NCS})_2]^{2+}$ unit and two nitrates. In case of **3b** chloride ions and lattice trapped MeOH and H_2O molecules were utilized to crystallize the Ni_4 aggregate. Both the cationic complexes **3a** and **3b** were not crystallized as their thiocyanato salts in presence of stoichiometric excess of SCN^- ions. There are two crystallographically inequivalent, but nearly identical, tetranuclear units per unit cell of **3b**. The molecular formula of **3a** and **3b** each contains two hydrolyzed ligand fragments H_2L2^- (Scheme 1), originating from the parent ligand through hydrolysis of one imine arm in presence of SCN^-

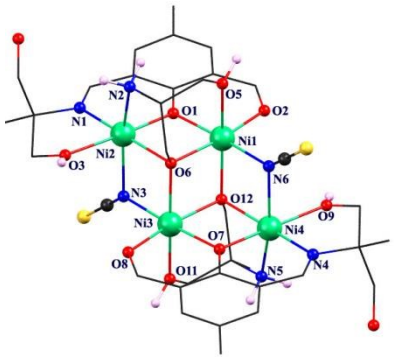

Figure 2. Molecular view of **3a** with partial atom numbering scheme. H-atoms are shown only for –OH and –NH_2 groups. Counter anions are omitted for clarity. Color code: Ni, green; N, blue; O, red; C, black; S, yellow; H, pink.

ions. These tetramers are centrosymmetric with a central core that can be described as a 'double-open' face-shared dicubane with two missing vertices. A different type of tetranuclear topology is thus obtained from the participation of SCN^- ions for coordination leading to ligand arm hydrolysis and coordination of aldehyde O in place of imine N. This caused coordination asymmetry within the $[Ni_2(H_2L2)(NCS)]^{2+}$ fragment with vacant sites around octahedral nickel(II) centers. To occupy those sites the liberated 2-amino-2-methyl-1,3-propanediol initially takes up $[Ni_2(H_2L2)(NCS)]^{2+}$ fragment through coordination from –OH and –NH_2 ends. The other –OH end following deprotonation trigger the aggregation of two such fragments by bridging three nickel(II) centers. Each hydrolyzed H_2L2^- entity provided O_3N donor set to the partial dicubane aggregate from the cooperative supports of two externally added SCN^- ions (N3 and N6) and liberated $HAMP^-$

View Article Online
DOI: 10.1039/C8NJ02695E

sets (N2, O5 and O6; N5, O11 and O12). Hydrolyzed asymmetric ligand fragment together with terminal coordination from SCN^- and tripodal $HAMP^-$ resulted NO_5 and N_3O_3 coordination spheres for two types of nickel(II) centers in **3a** (Figure 2) and **3b** (Figure S7 in the ESI†). Within these coordination spheres the Ni–O distances for terminal alcohol –OH arm remain within 2.094–2.120 Å range. Since **3a** and **3b** have similar cationic core structure, detail description for **3a** is only presented. Unlike **1** and **2**, the Ni–O distances are in 1.989–2.105 Å range and the Ni–N distances remain in 1.995–2.208 Å. Coordination of aldehyde group gave shortest Ni–O separation and Ni–O separation for terminal alcohol –OH arm is the longest one. In case of Ni–N distances, the bond to imine N is shortest and *apical* coordination from thiocyanate N provided longest separation. For **3a** the phenoxido-bridged Ni–O–Ni angles are in the range of 99.03–99.26° while the alkoxido-bridged Ni–O–Ni angles span within 97.14–100.57°. Interestingly, the thiocyanato-bridged Ni_2ON face recorded highest value of Ni–O–Ni angle (100.02 and 100.57°). The thiocyanato-bridging is typically unsymmetrical for two Ni–N_{NCS} bonds of 2.116–2.127 Å and 2.191–2.208 Å.[13] The Ni–N_{NCS}–Ni angles are 92.48° and 93.36°, different from the angles routinely obtained for symmetric faces.

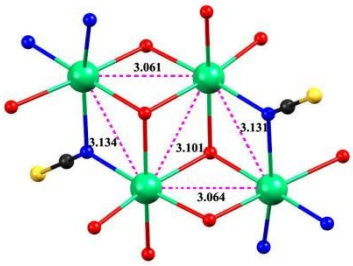

Figure 3 The Ni···Ni distances within the partial dicubane-like core of **3a**.

The Ni···Ni distances in five faces of the partial dicubane structure are different. For **3a** two phenoxido-alkoxido donor bearing faces (Ni–O–O–Ni diamond faces), also capped by $HAMP^-$, provided shortest Ni···Ni separations of 3.061 and 3.064 Å. The separation for the only double alkoxido ($HAMP^-$)-bridged face is 3.101 Å. While the presence of alkoxido ($HAMP^-$)-thiocyanato bridges gave longest separations of 3.131 and 3.134 Å (Figure 3). Long axis diagonal Ni2···N4 distance is 5.363 Å. The Ni2 and Ni4 centers are slightly strained from regular octahedral geometry compared to that of Ni1 and Ni3 (Table S1 in the ESI†).

For complex **3a**, coordinated hydroxyl arm engaged in hydrogen bonding interactions with nitrate counter anion (O9–H9···O18A). Second nitrate group showed such interactions (O5–H5···O15, O11–H11···O13) with trapped $HAMP^-$ unit following ligand arm hydrolysis. Such observation indicates the importance of these interactions for resultant stabilization of the aggregate and crystallization as nitrate salt. The favored development of the hydrogen-bonded 1D chain structure is possibly due to a stability of the 1D chain structure (Figure S8 in ESI†).

Likewise in **3b** the bound hydroxyl group from alcohol arm showed hydrogen bonding interaction with the chloride ion (O3A–H3A1···Cl2) as hydrogen bond acceptor. While the dangling hydroxyl group exhibit intermolecular hydrogen bonding interactions with another chloride ion (O4A–H4A···Cl1) as well as a coordinated hydroxyl group of the ligand alcohol arm of the second unit (O3B–H3B1···O4A, O3B–H3B1···O4B). Water molecules trapped within the crystal lattice further stabilize the structure by extending hydrogen bonding interactions with second chloride ion (O1W–H1W···Cl1) and bound hydroxyl group of $HAMP^-$ (O5A–H5A1···O1W). The bound amine end of $HAMP^-$ was further stabilized by participating in supramolecular hydrogen bonding interaction with chloride ion (N2B–H2B1···Cl2) (Figure S9 in ESI†).

Mass Spectroscopic Identification of the Fragments

High Resolution ESI-MS. The existence of different $Ni_2(H_4L1)$ and $Ni_2(H_2L2)$ based fragments in MeOH solutions were established from ESI-MS (positive) analysis of **1**, **2**, **3a** and **3b** (Figures S10-S15 in ESI†).

Complex 1. In MeOH solution **1** showed one intense peak at *m/z* = 529.06 (Calcd 529.06), attributed to acetate-bridged {Ni_2} fragment $[Ni_2(H_4L1)(OH)(O_2CCH_3)]^+$ ($C_{19}H_{29}N_2Ni_2O_8$). During crystallization two such fragments combine together to provide **1**. Two other small intensity peaks were observed at *m/z* values of 235.02 (Calcd 235.02) and 511.05 (Calcd 511.05), fitting nicely with the fragments $[Ni_2(H_4L1)(OH)]^{2+}$ ($C_{17}H_{26}N_2Ni_2O_6$) and $[Ni_2(H_2L1)(O_2CCH_3)\text{-}H]^+$ ($C_{19}H_{27}N_2Ni_2O_7$) respectively. Another small intensity peak appeared at *m/z* = 395.11 (Calcd 395.11) for the mononuclear species $[Ni(H_4L1)]^+$ ($C_{17}H_{25}N_2NiO_5$). Presence of these species in solution indicated that under suitable anion trapping and crystallization conditions, these fragments can possibly be isolated in the solid state.

Complex 2. In the spectra of **2** in MeOH solution, identifiable peaks of *m/z* values 235.02 and 395.11 can be assigned for fragments $[Ni_2(H_4L1)(OH)]^{2+}$ ($C_{17}H_{26}N_2Ni_2O_6$) and $[Ni(H_4L1)]^+$ ($C_{17}H_{25}N_2NiO_5$). In MeOH solution species like $[Ni_2(H_2L1)(O_2CC_2H_5)\text{-}H]^+$ ($C_{20}H_{29}N_2Ni_2O_7$) and $[Ni_2(H_4L1)(OH)(O_2CC_2H_5)]^+$ ($C_{20}H_{31}N_2Ni_2O_8$) showed peaks at *m/z* = 525.07 (Calcd 525.06) and 543.04 (Calcd 543.07) indicating the importance of carboxylate bridging for the {Ni_2} fragments before [Ni_4] aggregation. In this time the intensity of the former peak is medium, whereas of later it was small.

Complex 3a. In case of **3a** in MeOH the medium intensity peak at *m/z* = 468.05 (Calcd 468.03) can be assigned to dinuclear fragment $[Ni_2(HL2)(AMP)]^+$ ($C_{17}H_{24}N_2Ni_2O_6$). Other small-intensity peaks at *m/z* = 308.04 (Calcd 308.04) and 556.11 (Calcd 556.10) were assigned to the fragments $[Ni(H_2L2)]^+$ ($C_{13}H_{16}NNiO_4$) and $[Ni_2(H_2L2)(HAMP)(MeOH)(H_2O)_3]^+$ ($C_{18}H_{36}N_2Ni_2O_{10}$). Three other tetranuclear but degraded species were also observed in the MeOH solution of **3a.** These were $[Ni_4(L2)_2(AMP)]^{2+}$ ($C_{30}H_{37}N_3Ni_4O_{10}$), $[Ni_4(L2)_2(AMP)_2\text{-}H]^+$ ($C_{34}H_{47}N_4Ni_4O_{12}$) and $[Ni_4(HL2)_2(AMP)_2(NCS)]^+$ ($C_{35}H_{48}N_5Ni_4O_{12}S$) registering peaks at *m/z* = 416.51 (Calcd 416.49), 937.10 (Calcd 937.05) and 996.08 (Calcd 996.04) in the ESI-MS spectrum.

Complex 3b. Important fragments for **3b** closely resembled **3a** and only differ in signal intensity. Likewise peaks at *m/z* = 308.04, 416.51, 468.05, 556.11, 937.10 and 996.08 of **3b** in MeOH could be assigned to $[Ni(H_2L2)]^+$ ($C_{13}H_{16}NNiO_4$), $[Ni_4(L2)_2(AMP)]^{2+}$ ($C_{30}H_{37}N_3Ni_4O_{10}$), $[Ni_2(HL2)(AMP)]^+$ ($C_{17}H_{24}N_2Ni_2O_6$), $[Ni_2(H_2L2)(HAMP)(MeOH)(H_2O)_3]^+$ ($C_{18}H_{36}N_2Ni_2O_{10}$), $[Ni_4(L2)_2(AMP)_2\text{-}H]^+$ ($C_{34}H_{47}N_4Ni_4O_{12}$) and $[Ni_4(HL2)_2(AMP)_2(NCS)]^+$ ($C_{35}H_{48}N_5Ni_4O_{12}S$).

Proposed Routes for Two Types of Aggregation

Structurally characterized products obtained in this work and their disintegrations in solution clearly indicate the presence of molecular building fragments essential for aggregation reactions. Depending upon the nature of the fragments observed in mass spectroscopic analysis, we describe the growth of the aggregates from solution reactions and crystallization (Scheme 3). For **1** and **2**, the presence of carboxylate ions were responsible for the stabilization of both the imine arms and generation of HO^- ions to clip two nickel(II) ions in $[Ni_2(H_4L1)(\mu\text{–}OH)(\mu_{1,3}\text{–}O_2CCH_3)]^{2+}$. Condensation of two such fragments took place with the help of increase in bridging capacity (μ_2 to μ_3) of ligand phenoxido and ancillary hydroxido groups. On the other hand in the case of **3a** and **3b**, the chosen reaction protocol involving NH_4SCN *in lieu* of carboxylate anions lead to single imine arm hydrolysis and release of $HAMP^-$ for entrapment within **3a** and **3b**. Unlike in the previous case, now HO^- ions were not available for coordination and SCN^- ions were not able to bridge two nickel(II) ions. Instead the liberated amine alcohol showed unique bridging function within $[Ni_2(H_2L2)(HAMP)]^{2+}$ fragment. In the subsequent step two such fragments condensed through bridging by amine alkoxido part of amine alcohol and thiocyanato groups. To confirm the existence of $[Ni_2(H_2L2)(HAMP)]^{2+}$ in solution, we explored the single pot synthesis of **3a** and **3b** from preformed H_3L2 and external addition of H_2AMP.

Scheme 3 Two different routes of condensation reactions

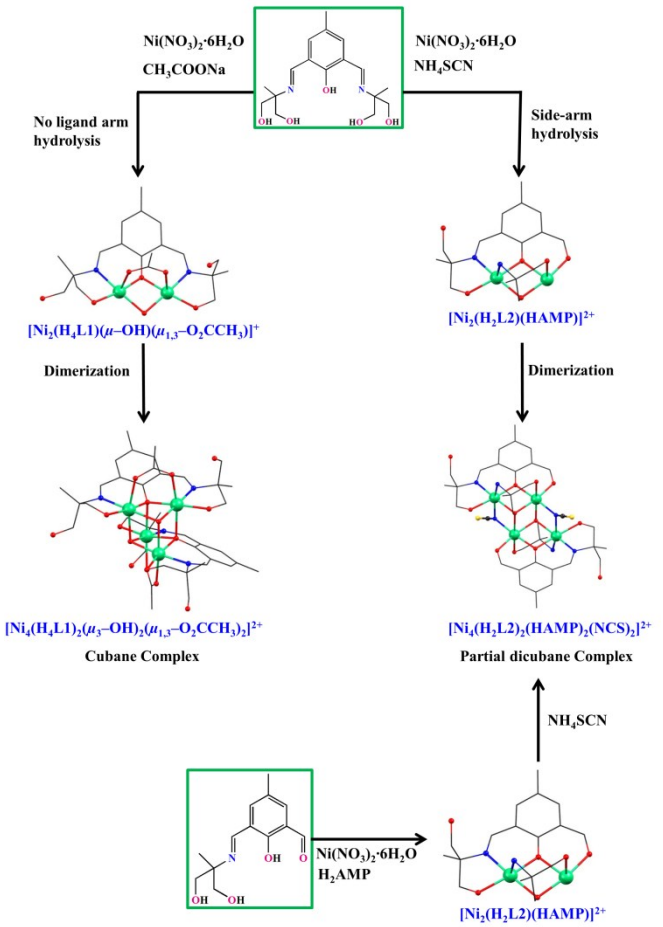

Magnetic Properties

The temperature and field dependent magnetic data of **1-3b** are depicted in Figure 4. The room temperature values of the effective magnetic moment μ_{eff} are in the range of 6.2–6.5 μ_B for all the compounds, and the decrease of μ_{eff} down to 1.9-4.2 μ_B is observed upon lowering the temperature to 2 K. Such behavior can be explained by prevailing antiferromagnetic interactions among nickel(II) paramagnetic centers within the $[Ni_4]$ molecular units, most probably accompanied by the zero-field splitting as well. This is evident also from the isothermal magnetizations measured at T = 2, 5 and 10 K, which do not saturate to the theoretical value of $M_{mol}/N_A\mu_B \rightarrow 4{\cdot}g{\cdot}S \approx 8$ assuming g = 2.0 and spin S = 1 per one nickel(II) center (Figure 4).

There are four nickel(II) atoms within the cubane core of the compounds **1** and **2** (Figures 1 and S4 in ESI†), thus the spin Hamiltonian contains six J_{ab}-parameters describing the exchange coupling as depicted in Figure 5.

$$\hat{H} = -J_{12}\left(\vec{S}_1 \cdot \vec{S}_2\right) - J_{13}\left(\vec{S}_1 \cdot \vec{S}_3\right) - J_{14}\left(\vec{S}_1 \cdot \vec{S}_4\right) - J_{23}\left(\vec{S}_2 \cdot \vec{S}_3\right) - J_{24}\left(\vec{S}_2 \cdot \vec{S}_4\right) - J_{34}\left(\vec{S}_3 \cdot \vec{S}_4\right) + \mu_B B \sum_{i=1}^{4} g_i \hat{S}_{z,i} \quad (5)$$

The complex **3a** with a partial dicubane geometry also contains four nickel(II) atoms (Figure 2), and thus the following spin Hamiltonian was postulated

$$\hat{H} = -J_{12}\left(\vec{S}_1 \cdot \vec{S}_2\right) - J_{13}\left(\vec{S}_1 \cdot \vec{S}_3\right) - J_{14}\left(\vec{S}_1 \cdot \vec{S}_4\right) - J_{23}\left(\vec{S}_2 \cdot \vec{S}_3\right) - J_{34}\left(\vec{S}_3 \cdot \vec{S}_4\right) + \mu_B B \sum_{i=1}^{4} g_i \hat{S}_{z,i} \quad (6)$$

where the exchange coupling between Ni2 and Ni4 was omitted due to large interatomic distance and lack of the suitable superexchange pathway. The situation is simpler in the case of the compound **3b**, because there are only two crystallographically independent nickel(II) atoms within the partial dicubane core (Figures S7 in ESI†) and thus, the spin Hamiltonian can be postulated in the following form

$$\hat{H} = -J_{11'}\left(\vec{S}_1 \cdot \vec{S}_{1'}\right) - J_{12}\left(\vec{S}_1 \cdot \vec{S}_2 + \vec{S}_{1'} \cdot \vec{S}_{2'}\right) - J_{12'}\left(\vec{S}_1 \cdot \vec{S}_{2'} + \vec{S}_{1'} \cdot \vec{S}_2\right) + \mu_B B \sum_{i=1}^{4} g_i \hat{S}_{z,i} \quad (7)$$

View Article Online
DOI: 10.1039/C8NJ03269F

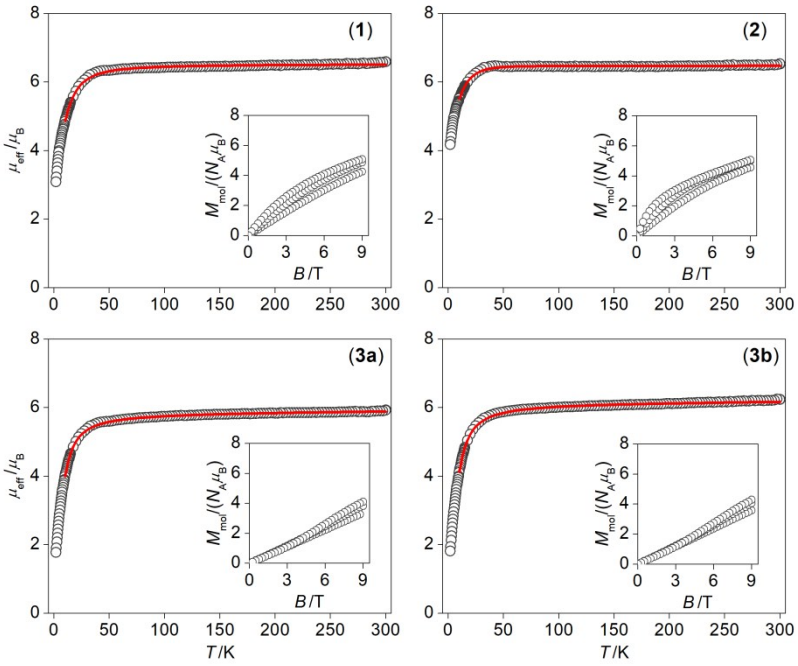

Figure 4 Magnetic properties of compounds **1**–**3b**. Each plot shows the temperature dependence of the effective magnetic moment, while the isothermal magnetizations measured at T = 2, 5 and 10 K are given in the inset. Experimental data – empty symbols, full lines – the best fit to magnetic data between 10 and 300 K calculated according to eqn. 1-3 with the parameters listed in the text.

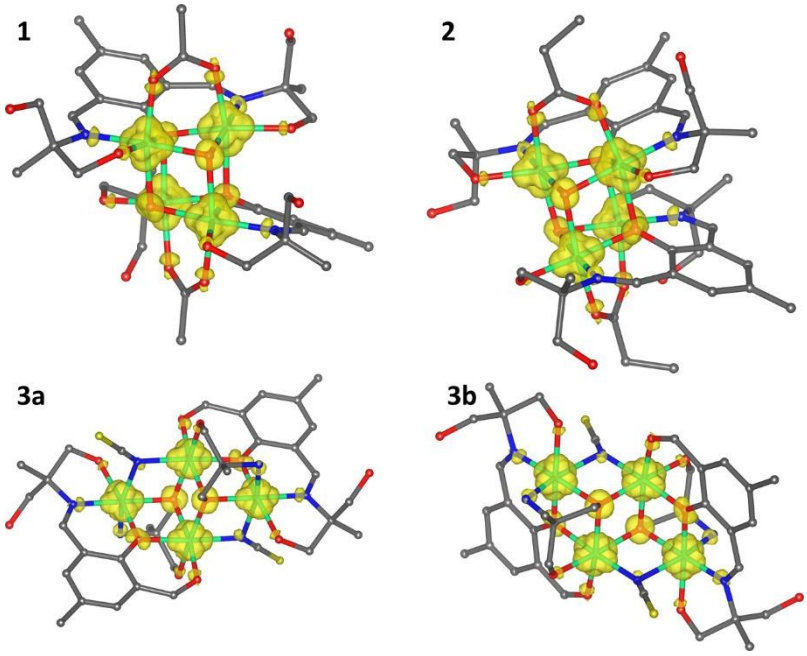

Figure 5 B3LYP calculated spin isodensity surfaces for high spin states with the cutoff values of 0.015 ea_0^3 for the molecular fragments $[Ni_4(H_4L1)_2(\mu_3\text{–}OH)_2(\mu_{1,3}\text{–}O_2CCH_3)_2]^{2+}$ of **1**, $[Ni_4(H_4L1)_2(\mu_3\text{–}OH)_2(\mu_{1,3}\text{–}O_2CC_2H_5)_2]^{2+}$ of **2**, $[Ni_4(H_2L2)_2(HAMP)_2(\mu_{1,1}\text{-}NCS)_2]^{2+}$ of **3a** and $[Ni_4(H_2L2)_2(HAMP)_2(\mu_{1,1}\text{-}NCS)_2]^{2+}$ of **3b**. Hydrogen atoms are omitted for clarity

To facilitate the analysis of the experimental magnetic data, the magneto-structural correlations can be utilized to minimize the number of the free parameters and avoid the over-parametrization of the model. Halcrow et al.[26] and later Meyer et al.[27] already established that the isotropic exchange in $[Ni_4]$ cubanes linearly correlates with the Ni–O–Ni angle. However, in the case of **1** and **2**, two pairs of the nickel(II) centers, Ni1-Ni2 and Ni3-Ni4, are also bridged by the acetate ligands, which means that the values of J_{12} and J_{34} cannot be solely determined from the Ni–O–Ni angles within this unit. Furthermore, there is no magneto-structural correlation confirmed for the partial dicubane topology.

Thus, the predictive role of DFT calculations in magnetochemistry was exploited with the aim to estimate principal parameters describing the exchange coupling in these molecular systems.[28] Recently, we used such approach for polynuclear Ni(II) complexes with the great success.[29,30,31] Therefore, well-established B3LYP functional was applied to

View Article Online
DOI: 10.1039/C8NJ03269F

calculate parameters of the isotropic exchange J_{ab} between the nickel(II) ions based on comparing the energy differences between the high spin (HS) and broken-symmetry (BS) spin states.[32] All theoretical calculations were performed with a freely available computational package ORCA employing the molecular geometries extracted from experimental X-ray data (Figure 5).

By the following Ruiz's approach[33,34] for the calculation of the *J*-parameters, these expressions for individual *J*-values were derived for complexes **1** and **2** with the cubane topology as

$$\begin{aligned} J_{12} &= (-\Delta_3 - \Delta_4 + \Delta_{13} + \Delta_{23})/6 \\ J_{13} &= (\Delta_1 + \Delta_3 - \Delta_{13})/6 \\ J_{14} &= (\Delta_1 + \Delta_4 - \Delta_{23})/6 \\ J_{23} &= (-\Delta_1 - \Delta_4 + \Delta_{13} + \Delta_{34})/6 \\ J_{24} &= (-\Delta_1 - \Delta_3 + \Delta_{23} + \Delta_{34})/6 \\ J_{34} &= (\Delta_3 + \Delta_4 - \Delta_{34})/6 \end{aligned} \quad (8)$$

where the energy differences are defined as $\Delta_{ij} = \varepsilon_{BSij} - \varepsilon_{HS}$. Then, the calculated J_{ij} parameters have the following values: J_{12} = +15.5 cm^{-1}, J_{13} = +5.8 cm^{-1}, J_{14} = +0.04 cm^{-1}, J_{23} = -0.01 cm^{-1}, J_{24} = -23.7 cm^{-1} and J_{34} = +15.9 cm^{-1} for **1**, and J_{12} = +14.6 cm^{-1}, J_{13} = +7.5 cm^{-1}, J_{14} = -2.6 cm^{-1}, J_{23} = -3.3 cm^{-1}, J_{24} = -19.8 cm^{-1} and J_{34} = +16.4 cm^{-1} for **2**. The relationship between J_{ab} and the structural parameters, namely the average Ni-O-Ni angle (α) and Ni···Ni distance (δ), is depicted in Figure 6.

When the J_{12} and J_{34} parameters affected by acetato co-bridging are excluded, the linear relationship between J_{ab} and α or even δ can be established for **1** and **2** (Figure 6)

$$J(\mathrm{cm}^{-1}) = 1126 - 11.3 \cdot \alpha(\mathrm{Ni\text{-}O\text{-}Ni}) \quad (9)$$

$$J(\mathrm{cm}^{-1}) = -1366 + 428 \cdot \delta(\mathrm{Ni\text{-}Ni}) \quad (10)$$

These results suggest that for α less than ≈ 100° and for δ larger than 3.2 Å, the ferromagnetic exchange is expected for the cubane motif. This agrees with theoretical expectations, because for the Ni-O-Ni angles close to the right angle, the magnetic orbitals based on d_{x2-y2} and d_{z2} of nickel ions are becoming orthogonal. The calculations also suggest that additional acetate-bridge strongly influences the exchange coupling and the J_{12} and J_{34} parameters are ferromagnetic and close to ≈ +15 cm^{-1} for both compound **1** and **2**. The broken-symmetry DFT approach was also applied to **3a** and the respective J_{ab} were derived with these equations

$$\begin{aligned} J_{12} &= (-\Delta_3 - \Delta_4 + \Delta_{13} + \Delta_{23})/6 \\ J_{13} &= (\Delta_1 + \Delta_3 - \Delta_{13})/6 \\ J_{14} &= (\Delta_1 + \Delta_4 - \Delta_{23})/6 \\ J_{23} &= (\Delta_3 - \Delta_4 + \Delta_{13} - \Delta_{23})/6 \\ J_{34} &= (-\Delta_1 + \Delta_4 + \Delta_{23})/6 \end{aligned} \quad (11)$$

As a result, the *J*-parameters adopted the values: J_{12} = -3.9 cm^{-1}, J_{13} = +7.3 cm^{-1}, J_{14} = +20.9 cm^{-1}, J_{23} = +23.6 cm^{-1} and J_{34} = -6.3 cm^{-1} for **3a**. Finally, these equations were derived for the compound **3b**

$$\begin{aligned} J_{11'} &= (-\Delta_{11'} + \Delta_{12} + \Delta_{12'})/6 \\ J_{12} &= (+\Delta_{11'} - \Delta_{12} + \Delta_{12'})/12 \\ J_{12'} &= (+\Delta_{11'} + \Delta_{12} - \Delta_{12'})/12 \end{aligned} \quad (12)$$

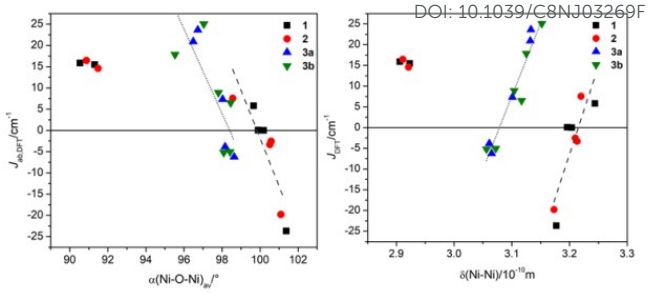

Figure 6 The magneto-structural data for **1-3b**, the dependence of DFT calculated J_{ab}-parameters on the average Ni-O-Ni angle α (left) and on the interatomic Ni•••Ni distance δ (right). The dashed lines correspond to linear correlations for **1-2** with the cubane geometry (eq 9-10), the dotted lines correspond to the linear correlations for **3a-3b** with partial dicubane geometry (eq 13-14)

The respective BS-DFT calculations were done for both Ni_4 clusters in the asymmetric unit of **3b**, which yielded $J_{11'}$ = +6.5 cm^{-1}, J_{12} = -5.2 cm^{-1}, $J_{12'}$ = +17.9 cm^{-1} and $J_{11'}$ = +8.9 cm^{-1}, J_{12} = -5.1 cm^{-1}, $J_{12'}$ = +25.0 cm^{-1}. All the calculated J_{ab}-parameters for **3a** and **3b** were included in the magneto-structural correlation, and it has been found that these values linearly correlate both with α and δ according to these equations

$$J(\mathrm{cm}^{-1}) = 978 - 9.94 \cdot \alpha(\mathrm{Ni\text{-}O/N\text{-}Ni}) \quad (13)$$

$$J(\mathrm{cm}^{-1}) = -1086 + 357 \cdot \delta(\mathrm{Ni\text{-}Ni}) \quad (14)$$

as depicted in Figure 6.

After establishing magneto-structural correlations between J_{ab} and average α(Ni-O/N-Ni) angles or δ(Ni···Ni) distances, we employed them in the fitting of the experimental magnetic data. But at first, here we also want to comment on the possibility that magnetic data at very low temperatures can be affected by the single-ion zero-field splitting of the respective nickel(II) centers. Generally, we can expect $|D_{Ni}|$ < 10-15 cm^{-1} for the hexacoordinate Ni(II) complexes[35,36] and due to heterogenous coordination sphere and the large deviations from the ideal octahedron, we can also expect non-negligible rhombicity (E/D > 0). Moreover, the local *D*-tensors must not be oriented in parallel fashion. All these facts show that inclusion of ZFS terms in the fitting procedure would results in large increase of the fitted parameters and the model would become easily over-parametrized. Therefore, the fits were done for the temperature dependent magnetic data above 10 K based on the isotropic spin Hamiltonians defined in eq 5-7. For all compounds, we utilized magneto-structural correlation based on the interatomic distance δ, because these data are slightly less scattered than those obtained from the α angle dependence (Figure 6). Thus, in the case of compounds **1** and **2**, there were five free parameters: the isotropic exchange between nickel(II) centres co-bridged by the acetate ligands was assumed for both couples to be the same $J_{12} = J_{34}$, the rest of J_{ab} were treated with linear equation analogous to eq 10, the same isotropic *g*-parameter was assumed for all the nickel atoms, and finally the temperature-independent

paramagnetism (TIP) was also added. The best fit for the complex **1** resulted in $J_{12} = J_{34} = 5.5$ cm^{-1}, $J_{ab} = -575 + 178{\cdot}\delta$, $g = 2.30$ and $\chi_{TIP} = 0.6$ m^{3}mol^{-1}. Then, the individual values of J_{ab} were: $J_{13} = 3.4$ cm^{-1}, $J_{14} = -5.2$ cm^{-1}, $J_{23} = -3.7$ cm^{-1}, $J_{24} = -8.6$ cm^{-1}. Analogous procedure for the complex **2** yielded $J_{12} = J_{34} = 8.3$ cm^{-1}, $J_{ab} = -994 + 310{\cdot}\delta$, $g = 2.25$ and $\chi_{TIP} = 5.0$ m^{3}mol^{-1} resulting in the individual values of J_{ab}: $J_{13} = 2.5$ cm^{-1}, $J_{14} = -0.56$ cm^{-1}, $J_{23} = 0.37$ cm^{-1}, $J_{24} = -12.0$ cm^{-1} (Figure 4). Next, the partial dicubane complexes **3a** and **3b** were fitted with four free parameters: all J_{ab} were treated with a linear equation analogous to eq 14, the same isotropic *g*-parameter was assumed for all nickel atoms and the TIP-parameter was also added. Then, the best fit for **3a** was obtained with $J_{ab} = -387 + 124{\cdot}\delta$, $g = 2.07$ and $\chi_{TIP} = 5.0$ m^{3}mol^{-1}. The individual values of J_{ab} were: $J_{12} = -6.2$ cm^{-1}, $J_{13} = -1.2$ cm^{-1}, $J_{14} = 2.6$ cm^{-1}, $J_{23} = 2.7$ cm^{-1}, $J_{34} = -5.7$ cm^{-1}. Finally, the parameters found for **3b** are $J_{ab} = -378 + 121{\cdot}\delta$, $g = 2.17$ and $\chi_{TIP} = 5.0$ m^{3}mol^{-1}. As there are two Ni_4 complexes within the asymmetric unit, the average Ni···Ni distance were used for δ-parameter. Then, the distinct J_{ab} are $J_{11'} = -0.71$ cm^{-1}, $J_{12} = -6.4$ cm^{-1}, $J_{12'} = 2.7$ cm^{-1} (Figure 4). The presented approach enabled to minimize the number of free parameters used for the analysis of the experimental magnetic data and resulted in reasonable sets of the parameters confirming that the complexes interplay between antiferromagnetic and ferromagnetic exchange interactions in **1-3b**.

Experimental Section

Materials. The solvents and chemicals used in this work were obtained from commercial sources, like SRL, India, Sigma-Aldrich, and Loba Chemie, India. Nickel nitrate, nickel chloride, sodium acetate, propionic acid and ammonium thiocyanate were obtained from SD Fine-chem Ltd and 2-amino-2-methyl-1,3-propanediol from Alfa Aesar. The chemicals used in this work were reagent-grade materials and were used as received without further purification. Sodium propionate, was prepared by treating propionic acid (0.15 g, 2.0 mmol) with sodium hydroxide (0.08 g, 2.0 mmol), followed by concentration and crystallization on a water bath. 2,6-diformyl-4-methylphenol (2-hydroxy-5-methyl-benzene-1,3-dicarbaldehyde) was prepared following a literature procedure.[37]

Synthesis of H_5L1 [2,6-bis-{(1,3-dihydroxy-2-methylpropan-2-ylimino)methyl)}-4-methylphenol]. H_5L1 was prepared by reacting 2,6-diformyl-4-methylphenol (0.820 g, 5mmol) with 2-amino-2-methyl-1,3-propanediol (1.05 g, 10mmol) in MeOH under room temperature stirring condition for 1 h followed by refluxing for 2 h. Removal of the solvent under vacuum yielded a yellow oily mass, which was characterized by FTIR and NMR spectroscopy. As obtained, oily product was dissolved in MeCN and used directly for reactions with metal salts without further purification. FT-IR (cm^{-1}, KBr pellet): 3341 (br), 1638 (m), 1219 (w), 1052 (w), 772 (vs). ^{1}H NMR (600 MHz, $(CD_3)_2SO$, δppm): 8.61 (2H, imine–H), 7.55 (2H, aromatic H), 3.42 (8H, –OCH_2), 2.50 (3H, –CH_3 substituent on phenyl ring), 1.18 (6H, –CH_3). ^{13}C NMR (150 MHz, $(CD_3)_2SO$, δppm): 163.58 (imine C), 124.78–160.01 (aromatic C), 66.06 (methylene C attached with O), 63.72 (tertiary C attached to imine N), 22.65 (methyl C attached with benzene ring), 18.63 (methyl C).

Synthesis of H_3L2 [3-{(1,3-dihydroxy-2-methylpropan-2-ylimino)methyl}-2-hydroxy-5-methylbenzaldehyde]. Drop wise addition of a MeOH solution (10 mL) of 2-amino-2-methyl-1,3-propanediol (0.21 g, 2mmol) to a MeOH solution (10 mL) of 2,6-diformyl-4-methylphenol (0.33 g, 2 mmol) under stirring condition followed by reflux for 2 h gave a light yellow solution. Cooling to room temperature followed by removal of solvent under vacuum yielded a yellow solid product of H_3L2. Yield: 0.235 g (94 %). This solid was characterized by FTIR, NMR spectroscopic analysis. FT-IR (cm^{-1}, KBr pellet): 3310 (br), 1663 (vs), 1647 (vs), 1528 (vs), 1229 (s), 1063 (m), 959 (m), 878 (w). ^{1}H NMR (400 MHz, $(CD_3)_2SO$, δppm): 10.33 (1H, aldehyde–H), 8.61 (1H, imine–H), 7.52-7.54(2H, aromatic H), 3.47 (4H, –OCH_2), 2.21 (3H, –CH_3 substituent on phenyl ring), 1.26 (3H, –CH_3). ^{13}C NMR (100 MHz, $(CD_3)_2SO$, δppm): 172.92 (imine C), 189.99 (aldehyde C), 118.81–164.26 (aromatic C), 65.04 (methylene C attached with O), 63.92 (tertiary C attached to imine N), 19.99 (methyl C attached with benzene ring), 18.05 (methyl C).

$[Ni_4(H_4L1)_2(\mu_3\text{–}OH)_2(\mu_{1,3}\text{–}O_2CCH_3)_2](NO_3)(CH_3COO){\cdot}3H_2O$ (1). To a stirred 'solution of H_5L1' (*approx*. 0.33 g, 1mmol) in MeCN (25 mL), next MeCN solution (25 mL) of $Ni(NO_3)_2{\cdot}6H_2O$ (0.580 g, 2mmol) was added. The resulting precipitated green solution was stirred for *ca*. 15 min. Methanolic solution (5 mL) of sodium acetate (0.164 g, 2mmol) was added to this green solution followed by NEt_3 (0.151 g, 1.5mmol) during which the color changes to deep green and the solution becomes clear and the stirring continued for next 2 h. The solution was filtered and kept for slow evaporation in air. The green single crystals suitable for X-ray analysis were obtained after 1 week. Yield: 0.438 g (71 %). Microanalytical data are consistent with the formula $[Ni_4(H_4L1)_2(\mu_3\text{–}OH)_2(\mu_{1,3}\text{–}O_2CCH_3)_2](NO_3)(CH_3COO){\cdot}3H_2O$ Anal. calcd. for $C_{40}H_{65}N_5Ni_4O_{24}$ (1234.78 g mol^{-1}): C, 38.91; H, 5.31; N, 5.67. Found: C, 39.01; H, 5.34; N, 5.68. Selected FT-IR bands: (KBr, cm^{-1}, vs = very strong, br = broad, s = strong, m = medium, w = weak) 3432 (br), 1645 (vs), 1628 (s), 1570 (s), 1384 (br), 1310 (s). UV-vis spectra [λ_{max}, nm (ε, L mol^{-1} cm^{-1})]: (MeOH solution) 994 (38), 760 (9), 622 (26), 368 (10200). Molar Conductance, Λ_M: (MeOH solution) 151 Ω^{-1} cm^2 mol^{-1}.

$[Ni_4(H_4L1)_2(\mu_3\text{–}OH)_2(\mu_{1,3}\text{–}O_2CC_2H_5)_2](NO_3)(C_2H_5COO){\cdot}CH_3CN{\cdot}1.5H_2O$ (2). Complex **2** was prepared following the similar procedure as described above for **1** by using sodium propionate (0.192 g, 2 mmol) in place of sodium acetate. Block shaped green crystals suitable for X-ray analysis was obtained from MeCN-MeOH (10:1) reaction mixture after 1 week. Yield: 0.446 g (69%). Anal. calcd for $C_{45}H_{72}N_6Ni_4O_{22.5}$ (1291.83 g mol^{-1}): C, 41.84; H, 5.62; N, 6.51. Found: C, 41.78; H, 5.62; N, 6.49. Selected FT-IR bands: (KBr, cm^{-1}, vs = very strong, br = broad, s = strong, m = medium, w = weak): 3460 (br), 1647 (vs), 1628 (s), 1570 (s), 1383 (br), 1307 (s). UV-vis spectra [λ_{max}, nm (ε, L mol^{-1} cm^{-1})]: (MeOH solution) 994 (36),762 (9), 622 (25), 368 (8000). Molar Conductance, Λ_M: (MeOH solution) 132 Ω^{-1} cm^2 mol^{-1}.

$[Ni_4(H_2L2)_2(HAMP)_2(\mu_{1,1}–NCS)_2](NO_3)_2$ (3a). Method A. Triggering of ligand hydrolysis. Complex **3a** was prepared following a similar procedure as described for **1** by using solid NH_4SCN (0.076 g, 1mmol) in place of sodium acetate. Green block shaped single crystals suitable for X-ray analysis was obtained after 6 days from this MeOH-MeCN (1:10) reaction mixture. Yield: 0.426 g (72%). Anal. calcd for $C_{36}H_{52}N_8Ni_4O_{18}S_2$ (1183.74 g mol^{-1}): C, 36.53; H, 4.43; N, 9.47. Found: C, 36.46; H, 4.38; N, 9.44. Selected FT-IR bands: (KBr, cm^{-1}, vs = very strong, br = broad, s = strong, m = medium, w = weak): 3411 (br), 2020 (vs), 1637 (vs), 1620 (vs), 1384(vs). UV-vis spectra [λ_{max}, nm (ε, L mol^{-1} cm^{-1})]: (MeOH solution) 983 (39), 596 (40), 395 (8500). Molar Conductance, Λ_M: (MeOH solution) 230 Ω^{-1} cm^2 mol^{-1}.

Method B. Direct use of H_3L2. MeCN solution (25 mL) of $Ni(NO_3)_2{\cdot}6H_2O$ (0.580 g, 2mmol) was added to a stirred solution of H_3L2 (0.235 g, 1 mmol) in MeCN (20 mL). The resulting clear green solution was stirred for ca. 15 min. Solid NH_4SCN (0.076 g, 1 mmol) was added to this followed by a MeOH solution (5 mL) of 2-amino-2-methyl-1,3-propanediol (0.105 g, 1 mmol). Addition of NEt_3 (0.303 g, 3 mmol) increases the intensity of the color of solution and further stirring was continued for 2 h. Green block shaped single crystals suitable for X-ray analysis was obtained from this reaction mixture after 6 days. Yield: 0.414 g (70%). Anal. calcd for $C_{36}H_{52}N_8Ni_4O_{18}S_2$ (1183.74 g mol^{-1}): C, 36.53; H, 4.43; N, 9.47. Found: C, 36.70; H, 4.40; N, 9.45. Selected FT-IR bands: (KBr, cm^{-1}, vs = very strong, br = broad, s = strong, m = medium, w = weak): 3411 (br), 2020 (vs), 1637 (vs), 1620 (vs), 1384(vs).

$[Ni_4(H_2L2)_2(HAMP)_2(\mu_{1,1}–NCS)_2]Cl_2{\cdot}CH_3OH{\cdot}H_2O$ (3b). Method A. Triggering ligand hydrolysis. Complex **3b** was obtained by doing the reaction in the similar line as chosen for **3a** by using $NiCl_2{\cdot}6H_2O$ (0.476 g, 2 mmol) in place of $Ni(NO_3)_2{\cdot}6H_2O$ in MeOH. Prismatic shaped green crystals suitable for X-ray analysis was obtained from the reaction mixture in MeOH after 12 days. Yield: 0.425 g (72%). Anal. calcd for $C_{37}H_{58}Cl_2N_6Ni_4O_{14}S_2$ (1180.75 g mol^{-1}): C, 37.64; H, 4.95; N, 7.12. Found: C, 37.58; H, 4.93; N, 7.11. Selected FT-IR bands: (KBr, cm^{-1}, vs = very strong, br = broad, s = strong, m = medium, w = weak): 3402 (br), 2018 (vs), 1637 (vs), 1620 (vs). UV-vis spectra [λ_{max}, nm (ε, L mol^{-1} cm^{-1})]: (MeOH solution) 974 (16), 592 (20), 395 (5400). Molar Conductance, Λ_M: (MeOH solution) 135 Ω^{-1} cm^2 mol^{-1}.

Method B. Direct use of H_3L2. Compound **3b** was also obtained following the same method used for **3a** using nickel chloride in place of nickel nitrate in MeOH. Prismatic shaped green crystals suitable for X-ray analysis was obtained from the reaction mixture after 12 days. Yield: 0.401 g (68%). Anal. calcd for $C_{37}H_{58}Cl_2N_6Ni_4O_{14}S_2$ (1180.75 g mol^{-1}): C, 37.64; H, 4.95; N, 7.12. Found: C, 37.61; H, 4.96; N, 7.11. Selected FT-IR bands: (KBr, cm^{-1}, vs = very strong, br = broad, s = strong, m = medium, w = weak): 3402 (br), 2018 (vs), 1637 (vs), 1620 (vs).

Physical Measurements

Elemental analyses (C, H and N) were performed with a PerkinElmer model 240C elemental analyzer. A Shimadzu UV 3100 UV–vis–NIR spectrophotometer and a PerkinElmer RX1 spectrometer were used to record the solution phase electronic absorption spectra and solid state FTIR spectra respectively. The phase purity of the powder compounds was determined by powder X-ray diffraction (PXRD) patterns using a Rigaku MiniFlex II desktop X-ray diffractometer (30 kV, 15 mA) using Cu-K_α radiation (λ = 1.5418 Å) within 5–50° (2ϑ) angular range and a fixed-time counting of 4 s at 25 °C. A Bruker esquire 3000 plus mass spectrometer was employed to collect the electrospray ionization (ESI) high resolution mass spectra of the four compounds. Electron paramagnetic resonance (EPR) spectra were recorded at 9.13 GHz (X-band) in continuous wave mode with a Bruker ELEXSYS 580 X-band EPR spectrometer equipped with a standard accessory for room temperature operation (298 K). Temperature dependent (T = 1.9 – 300 K, B = 0.1 T) and field dependent (B = 0 – 9 T, T = 2, 5 and 10 K) magnetic measurements were carried out on powder samples on a PPMS Dynacool system (Quantum Design) with a VSM option. The data were corrected for the diamagnetism of the constituents.

Theoretical calculations

The theoretical calculations were carried out with the ORCA 4.0 computational package.[38,39] B3LYP DFT functional[40,41,42] was used for calculations of the isotropic exchange constants J, following Ruiz´s approach,[43,44] by comparing the energies of high-spin (HS) and broken-symmetry spin (BS) states. The polarized triple-ζ quality basis set def2-TZVP proposed by Ahlrichs and co-workers was used for nickel and sulphur, def2-TZVP(-f) basis set for nitrogen and oxygen atoms and def2-SVP basis set for carbon and hydrogen atoms.[45] The calculations utilized the RI approximation with the decontracted auxiliary def2/J Coulomb fitting basis set[46] and the chain-of-spheres (RIJCOSX) approximation to exact exchange[47,48] as implemented in ORCA. Increased integration grids (Grid5 and Gridx5 in ORCA convention) and tight SCF convergence criteria were used in all calculations. The molecular fragment used in the calculations was extracted from the experimental X-ray. The calculated spin density was visualized with VESTA 3 program.[49]

Crystal Data Collection and Refinement

Single crystal X-ray diffraction data for **1**, **2** and **3a** were collected on a Bruker SMART APEX-II CCD X-ray diffractometer furnished with a graphite-monochromated Mo Kα (λ = 0.71073 Å) radiation by the ω scan (width of 0.3° $frame^{-1}$) method at 293 K for **1** and **2** and at 300 K for **3a** with a scan rate of 4 s per frame. SAINT and XPREP software[50] were used for Data processing and space group determination. Direct method of SHELXS-2014[51] were used to solve the structure and then refined with full-matrix least squares using the SHELXL (2014/7)[52] program package included into WINGX system Version 1.80.05.[53] Data were corrected for Lorentz and polarization effects; an empirical absorption correction was applied using SADABS.[54] For complex **3b**, the data were collected at 295 K using a Nonius Kappa CCD diffractometer. The dataset was integrated using the Denzo SMN package[55] and corrected for Lorentz, polarization and absorption effects

(SORTAV).[56] The structure was solved by direct methods (SIR97)[57] and the calculations were performed using SHELXL-2014/6[52] and PARST[58] implemented in WINGX suite of programs.[59] The locations of the heaviest atoms (Ni) were determined easily. The O, N, and C atoms were subsequently determined from the difference Fourier maps. These atoms are refined anisotropically. The H atoms were incorporated at calculated positions and refined with fixed geometry and riding thermal parameters with respect to their carrier atoms. Molecular structures were drawn using DIAMOND software.[60] A summary of the crystal data and relevant refinement parameters is given in Table S3 (ESI†). For complex **2**, O15 was refined over two positions as O15A (60% occupancy) and as O15B (40% occupancy). The decision to split the atom into two arises from the residual electron density peak Q1 (4.33 e/Å^{-3}) near C11 in the difference Fourier map when 100% occupancy was considered for O15A indicating the presence of static disorder of the oxygen atom. Crystallographic data (excluding structure factors) have been deposited with the Cambridge Crystallographic Data Centre as supplementary publications CCDC 1835111, 1835112, 1835113, 1835110. These data can also be obtained free of cost at www.ccdc.cam.ac.uk/conts/retrieving.html (or from the Cambridge Crystallographic Data Centre).

Conclusions

The varying reactivity patterns of ligand H_5L1 toward nickel(II) ions have been established during the synthesis of two new types of coordination aggregates. These are the new examples of synthesis controlled by the use of different anions in the reactions. For molecular aggregate formation the role of anions are crucial along with the nature of parent ligand system and metal ions for incorporation. The studied reactions in presence of two different anions followed by crystallizations have not provided any discrete [Ni_2] molecular complex. Only mass spectra analysis identified the {Ni_2} fragments responsible for facile and spontaneous self-aggregation reactions to provide **1**-**3b**. The X-ray structural analysis established the formation of the cubane type structures for **1** and **2** for first type of anions. Change in reaction conditions and use of thiocyanate anions led to partial hydrolysis of nickel(II) ion bound H_4L1^- to H_2L2^-, for defective dicubane structures in **3a** and **3b**. The solid-state studies of the magnetic properties were supported by DFT and provided a complete picture of the interplay between antiferromagnetic and ferromagnetic exchange interactions operating within complexes **1** to **3b**.

Conflicts of interest

The authors declare no competing financial interest

Acknowledgements

M.D. is grateful to IIT Kharagpur for her research fellowship. M.D. is thankful to Dr. K. L. Pruseth for his kind help in collecting PXRD data and Mr. Samiran Mishra for his help in PXRD data fitting. M.D. also acknowledges Dr. P. P. Jana for his valuable suggestions regarding X-ray structure solution. We are also thankful to DST, New Delhi, for providing the Single Crystal X-ray Diffractometer facility in the Department of Chemistry, IIT Kharagpur under FIST program. ZT and RH acknowledge financial support going from the National Programme of Sustainability I (LO1305) of the Ministry of Education, Youth and Sports of the Czech Republic.

References

1 C. Cadiou, M. Murrie, C. Paulsen, V. Villar, W. Wernsdorfer and R. E. P. Winpenny, *Chem. Commun*., 2001, 2666–2667.
2 H. E. Wages, K. L. Taft and S. J. Lippard, *Inorg. Chem*., 1993, **32**, 4985–4987.
3 M. Pait, A. Bauza, A. Frontera, E. Colacio and D. Ray, *Inorg. Chem*., 2015, **54**, 4709–4723.
4 D. Mandal, V. Bertolasi, J. Ribas-Arino, G. Aromi and D. Ray, *Inorg. Chem*., 2008, **47**, 3465-3467.
5 C. J. Milios and R. E. P. Winpenny, *Struct. Bond.*, 2015, **164**, 1–119.
6 K. Chattopadhyay, G. A. Craig, A. Kundu, V. Bertolasi, M. Murrie and D. Ray, *Inorg. Chem*., 2016, **55**, 10783-10792.
7 S. Carretta, P. Santini, G. Amoretti, M. Affronte, A. Candini, A. Ghirri, I. S. Tidmarsh, R. H. Laye, R. Shaw and E. J. L. McInnes, *Phys. Rev. Lett*.**,** 2006, **97**, 207201–207204.
8 Y. S. Moroz, S. Demeshko, M. Haukka, A. Mokhir, U. Mitra, M. Stocker, P. Muller, F. Meyer and I. O. Fritsky, *Inorg. Chem*., 2012, **51**, 7445–7447.
9 M. Manoli, A. Collins, S. Parsons, A. Candini, M. Evangelisti and E. K. Brechin, *J. Am. Chem. Soc*., 2008, **130**, 11129–11139.
10 D. L. Reger, A. E. Pascui, P. J. Pellechia, M. D. Smith, J. Jezierska and A. Ozarowski, *Inorg. Chem*., 2014, **53**, 4325−4339.
11 S. S. Tandon, S. D. Bunge, R. Rakosi, Z. Xu and L. K. Thompson, *Dalton Trans*., 2009, 6536–6551.
12 Y.-Z. Gao, Y.-A. Zhang and J. Zhang, *Inorg. Chem. Commun*., 2015, **54**, 85–88.
13 T. Singha Mahapatra, S. Chaudhury, S. Dasgupta, V. Bertolasi and D. Ray, *New J. Chem*., 2016, **40**, 2268−2279.
14 S. Petit, P. Neugebauer, G. Pilet, G. Chastanet, A.-L. Barra, A. B. Antunes, W. Wernsdorfer and D. Luneau, *Inorg. Chem*., 2012, **51**, 6645−6654.
15 J. Esteban, E. Ruiz, M. Font-Bardia, T. Calvet and A. Escuer, *Chem. Eur. J*., 2012, **18**, 3637–3648.
16 S. Chattopadhyay, M. G. B. Drew, C. Diaz and A. Ghosh, *Dalton Trans*., 2007, 2492**–**2494.
17 D. Maity, S. Chattopadhyay, A. Ghosh, M. G. B. Drew and G. Mukhopadhyay, *Inorg. Chim. Acta*, 2011, **365**, 25–31.
18 P. Bhowmik, S. Chattopadhyay, M. G. B. Drew, C. Diaz and A. Ghosh, *Polyhedron*, 2010, **29**, 2637–2642.
19 L. Li, S. Chen, R.-M. Zhou, Y. Bai and D.-B. Dang, *Spectrochim. Acta A*, 2014, **120**, 401−404.
20 M. Moragues-Canovas, M. Helliwell, L. Ricard, E. Riviere, W. Wernsdorfer, E. Brechin and T. Mallah, *Eur. J. Inorg. Chem*., 2004, 2219−2222.
21 G. Abbas, Mariya-al-Rashida, A. Irfan, U. A. Rana and I. Shakir, *J. Struct. Chem*., 2014, **55**, 30−37.
22 R. M. Buchanan, M. S. Mashuta, K. J. Oberhausen, J. F. Richardson, Q. Li and D. N. Hendrickson, *J. Am. Chem. Soc*., 1989, **111**, 4497−4498.

23 S. Mandal, V. Balamurugan, F. Lloret and R. Mukherjee, *Inorg.Chem*., 2009, **48**, 7544−7556.
24 E. I. Solomon and A. B. P. Lever, Inorganic Electronic structure and Spectroscopy, Wiley, New York, 1999.
25 A. K. Ghosh, A. Bauza, V. Bertolasi, A. Frontera and D. Ray, *Polyhedron*, 2013, **53**, 32−39.
26 M. A. Halcrow, J.-S. Sun, J. C. Huffman and G. Christou, *Inorg. Chem*., 1995, **34**, 4167–4177.
27 A. Das, F. J. Klinke, S. Demeshko, S. Meyer, S. Dechert and F. Meyer, *Inorg. Chem*., 2012, **51**, 8141–8149.
28 R. Herchel, I. Nemec, M. Machata and Z. Trávníček, *Inorg. Chem.*, 2015, **54**, 8625–8638.
29 I. Nemec, R. Herchel, M. Machata and Z. Trávníček, *New J. Chem.*, 2017, **41**, 11258–11267.
30 M. Machata, I. Nemec, R. Herchel and Z. Trávníček, *RSC Adv.*, 2017, **7**, 25821–25827.
31 R. Herchel, I. Nemec, M. Machata and Z. Trávníček, *Dalton Trans*., 2016, **45**, 18622–18634.
32 F. Neese, *Coord. Chem. Rev*., 2009, **253**, 526–563.
33 E. Ruiz, A. Rodríguez-Fortea, J. Cano, S. Alvarez and P. Alemany, *J. Comput. Chem*., 2003, **24**, 982–989.
34 E. Ruiz, J. Cano, S. Alvarez and P. Alemany, *J. Comput. Chem*., 1999, **20**, 1391–1400.
35 J. Titiš and R. Boča, *Inorg. Chem.*, 2010, **49**, 3971–3973.
36 R. Boča, *Coord. Chem. Rev.*, 2004, **248**, 757–815.
37 R. R. Gagne, C. L. Spiro, T. J. Smith, C. A. Hamann, W. R. Thies and A. D. Shiemke, *J. Am. Chem. Soc.*, 1981, **103**, 4073−4081.
38 F. Neese, Wiley Interdiscip. Rev.: Comput. Mol. Sci., 2012, **2**, 73–78.
39 F. Neese, *Wiley Interdiscip. Rev*.: *Comput. Mol.Sci*., 2018, **8**, e1327.
40 A. D. Becke, *Phys. Rev. A*, 1988, **38**, 3098-3100.
41 C. Lee, W. Yang and R. G. Parr, *Phys. Rev. B*, 1988, **37**, 785-789.
42 P. J. Stephens, F. J. Devlin, C. F. Chabalowski and M. J. Frisch, *J. Phys. Chem*., 1994, **98**, 11623–11627.
43 E. Ruiz, J. Cano, S. Alvarez and P. Alemany, *J. Comput. Chem*., 1999, **20**, 1391–1400.
44 E. Ruiz, A. Rodriguez-Fortea, J. Cano, S. Alvarez and P. Alemany, *J. Comput. Chem*., 2003, **24**, 982-989.
45 F. Weigend and R. Ahlrichs, *Phys. Chem. Chem. Phys*., 2005, **7**, 3297–3305.
46 F. Weigend, *Phys. Chem. Chem. Phys*., 2006, **8**, 1057–1065.
47 F. Neese, F. Wennmohs, A. Hansen and U. Becker, *Chem. Phys*., 2009, **356**, 98–109.
48 R. Izsak and F. Neese, *J. Chem. Phys*., 2011, **135**, 144105/1–144105/11.
49 K. Momma and F. Izumi, *J. Appl. Crystallogr*., 2011, **44**, 1272-1276.
50 *SAINT, SMART and XPREP*, Siemens Analytical X-ray Instruments Inc., Madison, WI, 1995.
51 G. M. Sheldrick, *SHELXS-2014*, *Program for Crystal Structure Solution*, University of Göttingen, 2014.
52 G. M. Sheldrick, Crystal structure refinement with SHELXL. *Acta Crystallogr.,Sect. A: Found. Crystallogr*., 2008, **64**, 112−122.
53 L. J. Farrugia, *WinGX-Version 2014.1*, *J. Appl. Crystallogr*., 2012, **45**, 849−854.
54 G. M. Sheldrick, *SADABS Software for Empirical Absorption Correction*, University of Göttingen, Institute für Anorganische Chemieder Universität, Göttingen, Germany, 1999−2003.
55 Z. Otwinowski and W. Minor, Processing of X-ray Diffraction Data Collected in Oscillation Mode, in *Methods in Enzymology: Macromolecular Crystallography, part A*, ed. Carter Jr, C. W.; Sweet, R. M. Academic Press, New York, 1997, **276**, 307–326.
56 R. H. Blessing, Acta Crystallogr., Sect. A: Found. Crystallogr., 1995, **51**, 33–37.
57 A. Altomare, M. C. Burla, M. Camalli, G. L. Cascarano, C. Giacovazzo, A. Guagliardi, A. G. G. Moliterni, G. Polidori and R. J. Spagna, *J. Appl. Crystallogr*., 1999, **32**, 115–119.
58 M. Nardelli, *J. Appl. Crystallogr*., 1995, **28**, 659.
59 L. J. Farrugia, *J. Appl. Crystallogr*., 1999, **32**, 837–838.
60 *DIAMOND*, *Visual Crystal Structure Information System, version 3.1*, Crystal Impact: Bonn, Germany, 2004.

View Article Online DOI: 10.1039/C8NJ03269F

View Article Online
DOI: 10.1039/C8NJ03269F

Table of Contents

Anion Coordination Directed Synthesis Patterns for [Ni_4] Aggregates: Structural Changes for Thiocyanate Coordination and Ligand Arm Hydrolysis

Manisha Das,[a] Radovan Herchel,[b] Zdeněk Trávníček,[b] Valerio Bertolasi,[c] and Debashis Ray*[,a]

Competitive bridging modes of HO^- and NCS^- were explored for four Ni^{II}-based coordination aggregates in cubane and dicubane topology.